CFD-based Development of an Ignition Chamber for a lean and high efficient CNG Combustion

G. Lucas, G. Tallu, M. Weißner

Volkswagen AG, Brieffach 011/1778, 38436 Wolfsburg, Germany

E-mail: gwendal.lucas@volkswagen.de
Telephone: +(49)5361-9-36357
Fax: +(49)5361 9-5736357

Abstract. The automotive industry considers internal combustion engines running on natural gas as a promising alternative to reduce CO_2-emissions. In this context, an innovative monovalent CNG engine based on an ultra-lean combustion process is developed. The latter uses a scavenged ignition chamber at nearly stoichiometric conditions to ensure a stable combustion of the lean mixture in the main chamber. A base configuration for the ignition and combustion chambers defined in a preliminary CFD investigation already delivers a break thermal efficiency of 43% in a modified diesel engine. The further improvement of such a concept by means of CFD simulations requires the development of a detailed spark ignition model. The latter considers the three phases of ignition, and is able to capture the effects of the turbulent flow field on the ignition process. The complete CFD model of ignition and combustion is implemented in the 3D-CFD software VECTIS, and is validated on the basis of engine measurements. The simulation results confirm the necessity of such a detailed ignition model in combustion simulations, as it is able to predict the onset of the particular restrike effect. The influence of the ignition chamber and the piston bowl designs on the combustion process are then separately investigated. The simulation results confirm that the geometry of both components constitute significant levers to improve the combustion efficiency. A final variation of the ignition chamber and piston bowl geometries allows the definition of the most advantageous combination in terms of efficiency and THC emissions for this engine concept.

1. Introduction

The automotive industry is facing tougher CO_2 and emission regulations. Besides pushing on electrification, a decarbonization of the internal combustion engine will remain important over the next decades. An advantageous pathway to significantly reduce CO2 emissions in internal combustion engines is the use of compressed natural gas (CNG), which offers a 25% CO_2 reduction compared to gasoline. CNG also offers a high heating value and a very high knock resistance, which can be exploited by designing a dedicated, monovalent engine, which does not need any compromises to run on gasoline, and offers an additional CO_2 advantage. In the EU funded project GasOn (project #652816, Horizon2020) several technologies like port injection, direct injection and ignition chamber concepts are investigated. This paper shows results from a further step towards the highest engine thermal efficiency, namely the development of a very lean CNG combustion process. To create a safe and robust inflammation for the hardly ignitable lean mixture, an ignition chamber has been configured. This concept is well known from the large bore low speed two-stroke stationary engines for example at MAN and it has been investigated, if such technology is feasible for a 2.0 litre CNG engine.

2. Ignition chamber concept

The ultra-lean combustion of an CNG-air-mixture faces two limits of ignitability: high pressure and high air-fuel ratio. The envisaged combustion concept offers both challenges at the same time due to a very short ignition delay causing a later ignition timing, hence a higher internal pressure at the time of ignition. In combination with relative air-fuel ratios around two, it is not possible to create a stable inflammation and combustion by a conventional spark. A new system offering a significantly higher ignition energy is required. The solution is the use of an ignition chamber. Fig. 1 illustrates this ignition concept.

The system contains two separate combustion chambers including two separate CNG feeds. A spark plug is located in the ignition chamber. The main combustion chamber is supplied with air, and the dominant mass of CNG conventionally via the inlet ports and a port injection. The mixture can reach air-fuel ratios larger than two. During compression, a part of the lean mixture flows into the ignition chamber. In this condition, the pressurised lean mixture in the ignition chamber cannot be ignited by the spark plug. In the next step, a very small amount of CNG is added via the separate dosing system into the ignition chamber to create a nearly stoichiometric mixture inside the ignition chamber. From this moment on, the spark plug

is able to ignite the mixture inside the ignition chamber, which starts burning and creates highly energetic flame jets, entering the main combustion chamber through the nozzles drilled in the ignition chamber. These flame jets offer enough energy to start the inflammation and guarantee the complete combustion of the ultra-lean mixture in the main chamber.

The previous process is the target combustion system, using the ignition chamber as a scavenged chamber. This means, that additional CNG is actively dosed into the chamber to create the envisaged stoichiometric mixture. A second way of using the ignition chamber is the unscavenged process without the additional dosing of CNG. This effect has also been investigated but is not part of this paper.

The package of this kind of ignition system was a challenge, due to the fact that the base engine is a Diesel engine. The straight valve orientation offers only a minimum space in the cylinder head to package all the components like the ignition chamber, spark plug, check valve, dosing system and a cooling system. A sample of an intermediate version is shown in Fig. 1. All components had to be packaged within the space, that is usually used by the diesel injector.
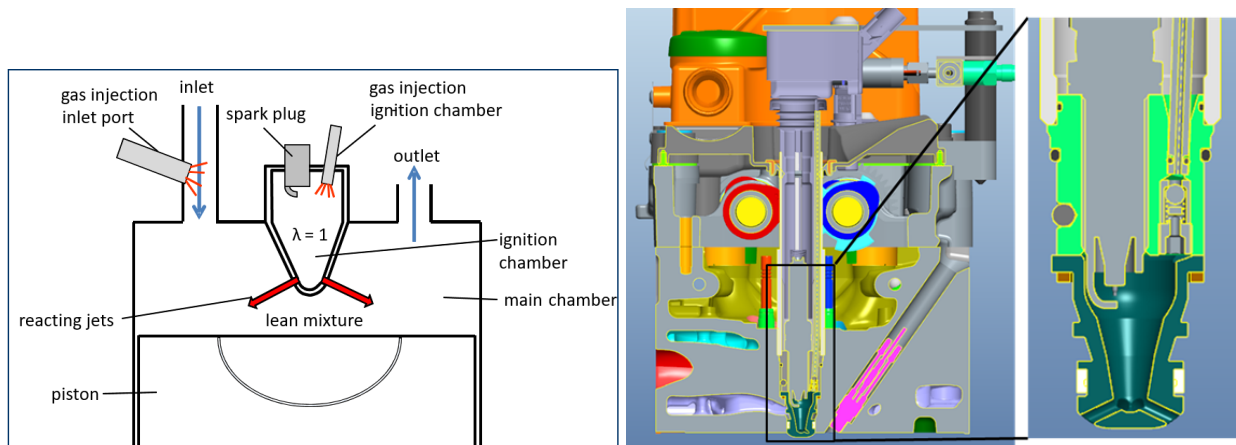

Fig. 1: Scheme of ignition chamber for ultra-lean CNG combustion(left), package of the ignition chamber into the cylinder head of a VW 2.0L TDI® engine(right)

At the start of the project, a first CFD setup has been used to investigate several ignition chamber geometries. For this purpose, the shape of the chamber, its internal volume, and several nozzle parameters such as the number, the orientation and the diameter, have been varied. This preliminary investigation has resulted in a first hardware design, which has been used for the first engine test bench measurements. This reference design is characterized by a volume of 1.82ccm, and features 7 nozzles of 1.5mm diameter in a tilted arrangement which generates a swirl inside the ignition chamber during the compression stroke.

The initial CFD investigation effort was based on an unvalidated setup including some necessary simple hypotheses. One aim of this project was the improvement of the CFD software VECTIS, in order to allow a further optimisation of the ignition chamber system, and to reach the highest engine efficiency. Following chapters describe this effort in detail.

3. CFD modelling

This novel concept of CNG combustion process for automotive engines can be improved with the help of detailed Three Dimensional Computational Fluid Dynamics (3D-CFD) simulations of the engine process. Hence, in this project a dedicated development of CFD modelling is carried out. Moreover, a detailed spark ignition model, which caters to the effects of turbulence in the vicinity of the spark plug and detailed chemical kinetics, is developed and validated. In this and next section, the modelling approaches and their validations are presented in detail.

3.1. Modelling of combustion process

An industry standard RANS-based k-ϵ turbulence model is used for the simulation. Details of this turbulence model and its implementation in the software VECTIS can be found in [1],[2]. The CFD domain is discretized with the help of the finite volume approach. The before-mentioned equations in their integral form are solved on this discretized CFD domain. This approach realises the solution of the flow field in the engine processes.

The premixed combustion process in the engine is modelled with the help of the level set G-Equation approach. Here, a passive scalar G is introduced and its transport equation is solved. The solution gives the marching of the flame through a distribution of the domain in three zones of burnt, unburnt and reaction

zone depending upon the value of G. The reaction zone locates the current position of the flame [3]. Details and implementation of the G-Equation approach in the commercial CFD code VECTIS can be found in [3], [4], [2]. The closure of the transport equations for the passive scalar G is achieved with the help of a turbulent flame speed model (S_t), where the correlation between the laminar flame speed (S_l) and the in-cylinder turbulence is stated. The model suggested by Herweg et al. in [5] is utilised for this purpose. This model neglects the strain effects on the laminar flame speed, which is an important aspect for the current engine setup. Natural gas is represented by the properties of methane in the CFD simulation. The laminar flame speed for methane is modelled with the help of the correlation presented by Metghalchi et al. in [6], which is modified to expand its suitability as per given in [7],[2].

The combustion process stated in Section 2, where separated combustion takes place in two different volumes, can be modelled with the state-of-the-art combustion modelling approach for premixed combustion, which is described above. The attempts in the past in Jamrozik et al. [8] and Heyne et al. [9] confirm this approach, where in different 3D-CFD software, a fundamentally applicable model for premixed combustion is used for the simulation of similar combustion processes.

3.2. Spark ignition modelling

In the combustion modelling approach presented in section 3.1, ignition is achieved through the deposition of energy in a cell at a given point of time. It is considered that the ignition is always successful and hence, after reaching a predefined size, the flame kernel is assumed to be converted into a fully propagating flame. This ignition approach is not physical, and especially for the representation of ignition in the ignition chamber, it cannot be utilised, as due to its design, there can be a chance of turbulence abating the ignition process. For this purpose a novel ignition modelling based on the physics of ignition is developed. The following section describes the physics of spark ignition and outlines this novel modelling approach.

3.2.1 Physics of spark ignition

Spark ignition is a complex and short lived phenomenon which is explained by number of researchers in the past. Ignition process takes place in three different electrical phases viz., breakdown, arc discharge and glow discharge. With the help of electrical characteristics in these three phases, any ignition system can be represented. A typical current voltage plot over spark discharge time describing these three phases is shown in Fig. 2.
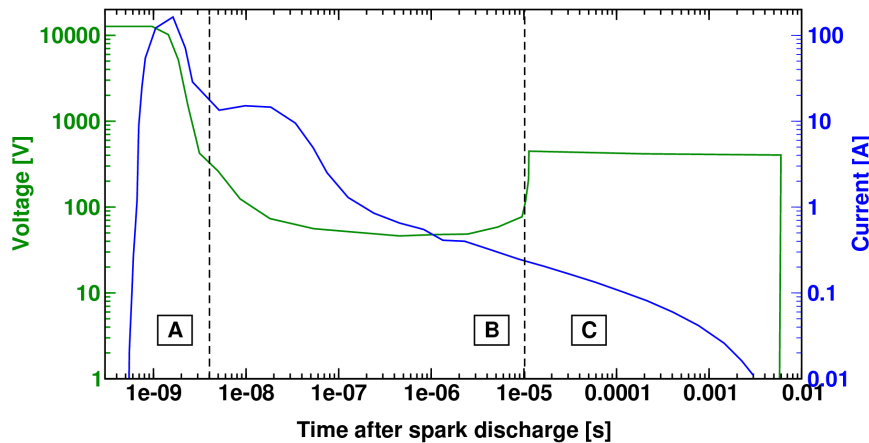

Fig. 2: Voltage and current during spark discharge for ignition process with A: Breakdown phase, B: Arc discharge phase, C: Glow discharge phase, from [10]

As the electrical energy is supplied to the spark plug electrodes, a tremendous rise in the voltage takes place. When this voltage exceeds the breakdown voltage ($\sim$ 15 kV), a short lived breakdown phase starts. In this duration, a rise in the current is also observed. During this phase, ionisation of the air-fuel mixture in the electrode gap and the subsequent plasma formation takes place. The plasma expands with supersonic speed and hence, it cools down [10].

The arc discharge phase is characterised by the drop in the voltage and the current, which is signified by the arcing taking place between the electrodes. This phase lasts for microseconds where, on the surface of the cooled plasma, initial radicals appear, such as C, N, O and H. They react with the radicals of N from surrounding, which initiate primary reactions of combustion. When the chemical energy support of these reactions is substantial, it is termed as a flame kernel [10].

Finally, during the glow discharge phase, where the visual glow of the spark is observed, the current drops even further till the order of milliamperes. But the voltage in this phase rises again till the secondary voltage, depending upon the inductance in the secondary circuit. This phase lasts for milliseconds but there is a very little electrical energy supply available for the inflammation. Hence, the flame kernel has to sustain on the chemical energy support from the combustion of air-fuel mixture in the surrounding. If the chemical energy support is sufficient enough to sustain against the turbulence in its vicinity, the flame kernel is transformed into a fully propagating flame [10].

3.2.2 Modelling approach

The challenge in the 3D-CFD modelling of spark ignition is the time and length scales under the consideration, which are very small compared to that of an engine simulation. Hence, there is a need to find the perfect trade-off between the modelling accuracy and the computational efforts to be invested for this purpose. It is possible to numerically model the process of plasma formation, expansion and subsequent flame kernel formation with the help of the Maxwell equations. This whole approach is presented by Thiele et al. in [11]. Here, the solution of electrical equations is coupled with a 3D-CFD simulation and reaction chemistry to get the effect of electrical energy deposition on the inflammation. However, as discussed in [11], a large computational effort is needed to solve the electrical equations and hence, the subsequent flame kernel simulations were restricted in the dimensional coordinates. The focus of the current work is rather on the simulation of the flame kernel and the subsequent flame propagation with the most thoroughness, hence such modelling approaches were not considered. The new modelling approach from [12] is depicted by Fig. 3.
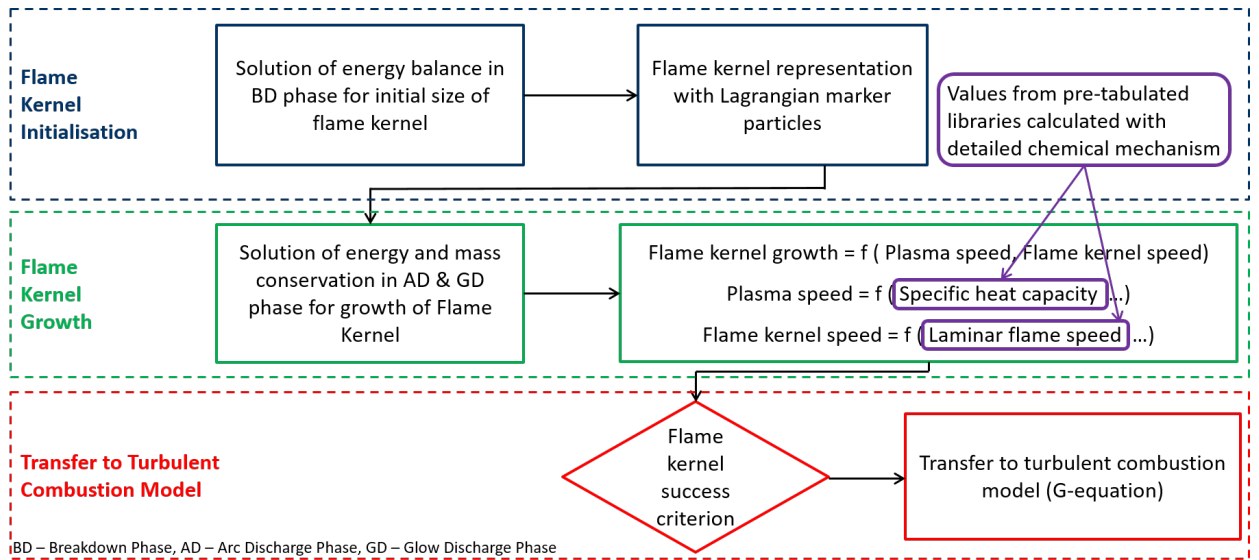

Fig. 3: Spark ignition modelling approach [12]

In the first submodel of flame kernel initialisation, the mass, size and temperature of the initial flame kernel are found out. For this purpose, the breakdown phase is considered as the combination of the ionisation stage and the plasma expansion stage. The ionisation stage is signified by the addition of breakdown energy E_{bd} to the plasma and a mass conservation. In the plasma expansion stage, the change in the volume of plasma takes place without any addition of external energy. Both of these stages can be represented with the help of the following scheme of equations:

$$\Delta E = c_{v1}\, m\, (T_1 - T_0) = E_{bd} + Q_{ch} \tag{1}$$

$$\Delta E = c_{v2}\, m\, (T_2 - T_1) + p_0\, (V_2 - V_0) = 0 \tag{2}$$

where, m is the mass of plasma, c_v is the specific heat at constant volume of the plasma, Q_{ch} is the chemical heat release with the burning of fuel, p is the pressure, v is the volume and T is the temperature at the conditions specified by the subscript 0 for ambient conditions, 1 for conditions at the end of ionisation phase and 2 for the conditions at the end of the expansion stage.

The solution of this system of equations leads to the initial value of the flame kernel radius r_k, which depends upon the ambient conditions, the spark plug electrode gap, the lower heating value of the fuel, the breakdown energy, the plasma specific heat which is derived from [13] and other parameters. The initial

spherical flame kernel of radius r_k is represented in the computational domain through lagrangian particles located at the centre of the spark plug electrode gap. Convectional effects of in-cylinder turbulence on the movement of the flame kernel are catered by the movement of the centre of these particles. At the new position, according to the size of the flame kernel at that point of time, the cluster of particles is again distributed.

The second submodel of flame kernel growth computes the change in flame kernel size in the arc and glow discharge phases. In these phases, the spark energy deposition, the flame kernel motion with burning of fresh air-fuel mixture from surrounding and the thermal diffusion of the kernel cause a change in the size of the flame kernel. Hence, the change in enthalpy of the flame kernel can be represented by:

$$\mathrm{d}H_k = Q_{sp} + V_k \, \mathrm{d}p_u \tag{3}$$

where, $\mathrm{d}H_k$ is the total change in enthalpy of the kernel with subscript k for flame kernel, V_k is the volume of spherical flame kernel, p_u is the ambient pressure and Q_{sp} is the electrical energy supplied by the ignition coil in this phase. The latter can be correlated with the spark power W and the spark duration t_{sp} through $Q_{sp} = W \cdot t_{sp}$. Similarly, the change in mass of the flame kernel (m_k) can be represented as:

$$\frac{\mathrm{d}m_k}{\mathrm{d}t} = \rho_u A_k \left(S_k + S_p\right) \tag{4}$$

where, ρ_u is the ambient density, A_k is the flame surface area of the flame kernel, S_k is the flame kernel speed, $C_{p,k}$ is the specific heat of kernel at constant pressure and S_p is the velocity contribution of plasma in the progress of flame kernel. The value of S_p can be found out by the solution of Eqn.4 with the assumption of no combustion and no change in the ambient conditions. In this way, Eqn.3 and 4 can be further simplified in the form of conservation equations as:

$$\frac{\mathrm{d}r_k}{\mathrm{d}t} = \frac{R_k \, T_k}{R_u \, T_u} \left(S_k + S_p\right) - \frac{r_k}{3} \left(\frac{1}{p_u} \frac{\mathrm{d}p_u}{\mathrm{d}t}\right)$$

$$\begin{aligned}
\frac{\mathrm{d}T_k}{\mathrm{d}t} = &\frac{3}{C_{p,k} \, r_k} \left(LHV_{mix} - \left(c_{p,k} \left(T_k - T_0^{std}\right) - c_{p,u} \left(T_u - T_0^{std}\right)\right)\right) \frac{R_k \, T_k}{R_u \, T_u} \left(S_k + S_p\right) \\
&+ \frac{W}{\frac{4}{3}\pi r_k^3 \, C_{p,u}} \frac{\gamma_k - 1}{\gamma_k} \frac{T_k}{R_u \, T_u} + \frac{\gamma_k - 1}{\rho_k} \frac{T_k}{p_u} \frac{\mathrm{d}p_u}{\mathrm{d}t}
\end{aligned} \tag{5}$$

where, T_0^{std} is the reference temperature of enthalpy formation, γ is the ratio of specific heat capacity and R is the gas constant. The closure of this system of equations is done by the model for S_k considering the curvature effects. This is represented as per [14], [15]:

$$S_k = S_t - \frac{2}{r_k} \left(\frac{\nu}{Pr_L} + C_c \, l_{ft} \, \nu'\right) \tag{6}$$

where, Pr_L is the Prandlt number, l_{ft} is the turbulent flame brush thickness and C_C is the mixing coefficient. S_t is modelled in the same way as given in section 3.1.

Detailed chemical kinetics are coupled to the spark ignition model in such a way that the values of $C_{p,k}$ and laminar flame speed for each cell under the flame kernel are read from pre-calculated tables. These values are calculated on the basis of a detailed kinetic mechanism for the combustion of natural gas, and are tabulated beforehand. In this work, rather, this coupling is not utilised.

Finally, in the submodel of transfer to the turbulent combustion model, based on the fulfillment of few criteria, the transfer of the flame kernel into a turbulent flame is catered. A first condition is based on the direct correlation between the growth of the flame kernel and the in-cylinder turbulence. For this purpose, a parameter defined as the critical flame kernel radius is calculated as:

$$r_{crit} = \mathsf{max}\left(2l_{fl} \quad , \quad \frac{2C_c \, l_{ft} \, \nu'}{S_t - S_l}\right) \tag{7}$$

where, l_{fl} is the laminar flame brush thickness. For the successful sustaining of the flame kernel, its radius should exceed this value at least at the end of discharge time. If this happens, then as discussed in Section 3.1, the level set G-Equation approach is started for the simulation of the flame progress.

A second criterion correlates the movement of the flame kernel due to in-cylinder turbulence. Here, the elongation of the spark channel is calculated as the length of the path connecting the anode and the cathode of the spark plug through the centre of the current position of the spherical flame kernel. If this path length is greater than the physical value of 10mm derived by Dahms et al. in [16], the restrike is initiated in the CFD domain. Here, the current flame kernel and its lagrangian marker particles are deactivated

and a new flame kernel is restarted from the centre of the spark plug electrode. The physical essence of restrike is that the strong turbulence in the proximity of the spark plug elongates the electrical path between the two electrodes. This effect excesses the resistance and hence, the electrical energy deposition for the inflammation of the surrounding air-fuel mixture. When the electrical energy is not sufficient to withhold this resistance, the electrical path is broken and a new contact between the electrodes is established. Details of this phenomena can be found in [16]. This concludes the modelling approach for ignition phenomenon. A validation of the whole modelling approach is presented in the next section.

4. Validation of ignition and combustion model

This section presents a validation of the above discussed models for ignition and combustion in the target engine setup. An extensive model validation of the spark ignition model has already been published by Tallu et al. in [12]. The reported results showed promising results, which motivated the application of this spark ignition model in the simulations of ignition chamber concepts.

4.1. Experimental setup

Before discussing the model validation, it is important to understand the base experimental setup. The above discussed engine concept is based on a commercial Volkswagen 2.0L TDI$^{®}$ engine, with a bore of 81 mm and a stroke of 95.5 mm. This engine is converted to be fuelled with an ultra-lean homogeneous mixture of air and natural gas. For this purpose, the base form of the ignition chamber described in Section 2 and shown in Fig. 4 is used. The piston bowl geometry is modified to an hemispherical form, as illustrated in Fig. 4. This changed the compression ratio of the engine to 14.5. Due to unforeseen charging problems, the engine is operated only in a restricted area of the engine map at various lean relative air-fuel ratios in the main chamber (λ_{CC}). For each operating point, the start (SOIg), the duration and the mass (MOIg) of natural gas injection in the ignition chamber is adjusted such that, a stoichiometric mixture at the spark ignition timing (ST) in the ignition chamber is always realised. The operating points (OP) shown in Table 1 are chosen for the CFD model validation. For the completeness of comparison, the last operating point OP D is computed by means of 1D-simulations. With the help of OP A, B and C, a variation only in the λ_{CC} is realised, while OP C and D only vary the engine speed. The spark timing is adjusted in such a way that the centre of combustion is always at 8°CA after Top Dead Centre (aTDC). Pressure sensors from Kistler are used to measure the pressure in the intake and exhaust manifolds, as well as in the cylinder and in the ignition chamber. At least 300 fired cycles are measured to get the averaged cyclic data for the purpose of validation.

Table 1: Selected engine operating points for CFD model validation

OP	Speed [rpm]	Load [Nm]	λ_{CC} [−]	SOIg [°CA]	Duration [°CA]	MOIg [mg]	ST [°CA aTDC]
A	1500	100	1.5	428	41	0.54	-8.5
B	1500	100	1.7	428	40	0.55	-11.5
C	1500	100	2.0	427	52	0.92	-15.5
D	4000	100	2.0	440	60	0.47	-25.0

4.2. Engine CFD setup

A short overview of the utilised 3D-CFD setup is hereafter given. The four-stroke cycle in a representative cylinder of the above discussed engine is simulated with the help of the 3D-CFD software VECTIS. For this purpose, the simulation domain consists of the intake port, the exhaust port, the main cylinder and the ignition chamber, as depicted in Fig. 4 by the cut through the central plane of the domain at Top Dead Centre (TDC). As seen in this figure, the inlet and exhaust ports are discretised with cartesian cells of size 2 mm. The cell size in the cylinder is of 1mm, while the cell size in the ignition chamber is 0.5 mm. The cells located in the nozzles area are further reduced to a size of 0.25 mm. The piston, intake and exhaust valves movements are considered and accordingly, the mesh is adjusted at approximately every 10°CA or at the point of time where these components show a large displacement. This discretisation strategy resulted in approximately 903000 cells at TDC and approximately 1080000 cells at Bottom Dead Centre (BDC). The mass flow rate at the intake manifold availed from 1D-CFD simulations is applied on the inlet boundary of the CFD domain. Here, the mixture composition is set to the predefined value of λ_{CC} for the operating point OP, as air and natural gas mixture induced in the cylinder is well premixed and homogeneous. On the

exhaust side, the averaged cyclic pressure measured in the experiments at the exhaust manifold is utilised. This strategy resulted in a deviation of less than 5% in the mass captured in the cylinder after intake valve closure than in the experiments. Natural gas injection in the ignition chamber is realised with the application of a mass flow rate obtained from 1D-CFD simulations at the inlet gas boundary in the ignition chamber. The simulation starts at the point of time when the exhaust valve is fully opened, and is continued till 80°aTDC. At the start of the simulation, the cylinder, the ignition chamber and the exhaust port are initialised with residual gas, while the intake port is initialised with the mixture composition corresponding to the λ_{CC} of the investigated operating point. In order to achieve stable simulations, the time step discretisation is chosen such that, the overall simulation is carried out with a time step of 0.02°CA, while during gas injection in the ignition chamber and combustion smaller time steps of 0.01°CA are applied. Depending upon the spark ignition duration, the smallest time step chosen for the operating points with the least engine speed of 1500 RPM is of 0.005°CA. The ignition process initiated by the set of ignition coil and spark plug in the engine experiments is reproduced in the experiments in the small volume of ignition chamber as given in [17]. The parameters required for the spark ignition model are availed from these experiments.
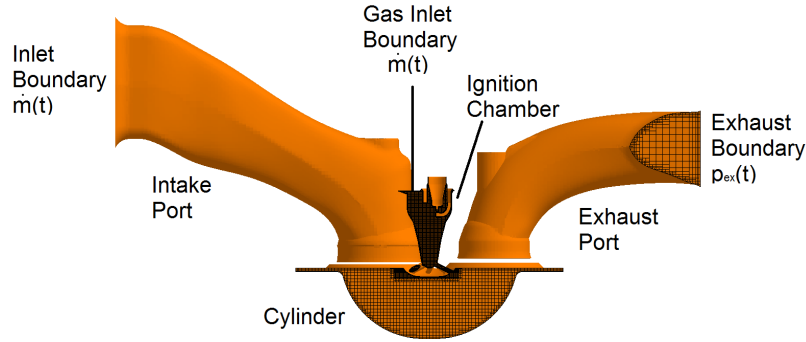

Fig. 4: Representation of engine setup in CFD domain with Cartesian mesh at TDC

4.3. Discussion of results

The results of validation are presented in two separate parts, viz. a variation in relative air-fuel ratio in the main chamber and an engine speed variation. With the help of the first variation, the modelling approaches for the ignition and combustion process are validated. The variation in engine speed enables a detailed study of the results computed by the spark ignition model.

4.3.1 Variation in relative air-fuel ratio

The operating points A, B and C vary the premixed air-fuel ratio in the main chamber λ_{CC} from 1.5 to 2.0. The measured and simulated pressure curves in the ignition and main chambers are shown in Fig. 5. For both pressure curves, the arrows show the spark timings applied in the individual operating points.
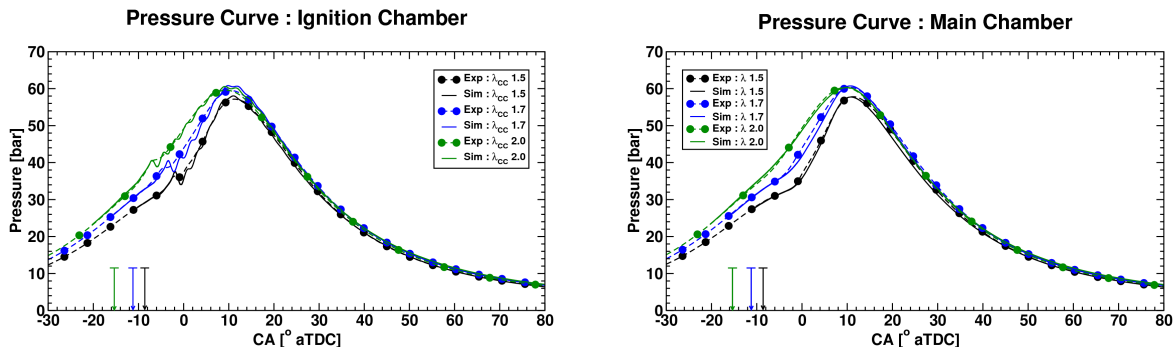

Fig. 5: Comparison of pressure curves of experimental data and simulation results for ignition chamber (Left) and main chamber (Right) of OP A (λ_{CC} 1.5), OP B (λ_{CC} 1.7) and OP C (λ_{CC} 2.0)

Due to the small absolute volume of the ignition chamber, the difference in pressure between the ignition and the main chambers is very limited. It can be observed that as the mixture gets leaner, the spark timing is advanced. Furthermore, for the leaner mixture, a higher air mass is required, which results in a larger

charging pressure. Both effects yield to an ignition taking place between 27 to 29 bar for these 3 operating points. The maximum pressure in the main and ignition chambers increases with the leaning of the mixture from 1.5 to 1.7, but from here onwards it remains constant.

Considering the ignition chamber, a good agreement is observed between the experimental data and the simulation results for the three operating points. The ignition phase, considered as the period from spark timing till the first peak in the pressure curve, is reproduced accurately by the simulations. In the next phase of combustion till the maximum pressure, fluctuations in the simulated curves are observed, which are not present in the experimental data. These fluctuations are the results of pressure waves travelling between the main and ignition chambers. The results of simulation are averaged over the whole volume of the ignition chamber, whereas, the pressure sensor is mounted at the top of the ignition chamber. Therefore, these waves show their effects only in the results of simulations. The computations reproduce with accuracy the timing and the value of the maximum pressure, as well as the results measured in the expansion stroke.

A similar agreement between experimental data and simulation results is observed for the main chamber pressure curve. The start of combustion, here taking place with the jets exiting from ignition chamber, is reproduced with accuracy. In the phase between the start of combustion and the maximum pressure, small deviations between the simulation results and the experimental data are observed, but the timings of the maximum pressures and their values are reproduced correctly in the simulations. In the expansion phase, except for the richest mixture, a good accordance between the considered results is observed.

In order to assess the results of the spark ignition model, the pressure curve of the ignition chamber is evaluated with the help of 3 parameters. They are, the time required for 10% pressure rise compared to the first pressure peak from spark timing ($|\alpha_{p10} - \text{ST}|$), the value of the first pressure peak (p_{peak}) and its timing (α_{peak}). These parameters help in the evaluation of the ignition occuring in the ignition chamber only. Table 2 presents for the three investigated operating points the values of these 3 parameters for the experimental data and the simulation results.

Table 2: Comparison of measured and simulated ignition parameters for the operating points OP A, OP B and OP C

OP		$|\alpha_{p10} - \text{ST}|$ [°CA]	p_{peak} [bar]	α_{peak} [°CA aTDC]
OP A	Exp	1	36.34	-1.8
	Sim	1.06	36.57	-1.9
OP B	Exp	0.9	38.68	-3.5
	Sim	1.04	40.44	-3.6
OP C	Exp	1.1	40.79	-6.1
	Sim	1.03	40.59	-6.3

Here it can be seen that, apart from few exceptions, the spark ignition model is able to reproduce the experimental results. For the first parameter $|\alpha_{p10} - \text{ST}|$, which is equivalent to an ignition delay, the maximum deviation observed between the simulations and the measurements remains lower than 7%. The values of this parameter vary in a very small range over the three operating points. This is mainly due to the fact that, irrespective of changes in the mixture composition in the main chamber, the conditions at the spark plug are similar for the three operating points. The value and the timing of the first pressure peak show the effect of change in mixture composition in the main chamber, where, with the increase in λ_{CC}, an increase in the first peak pressure and a delay in its timing is observed. This is mainly due to the change in the spark ignition timing according to the operating points. Apart from the peak pressure for OP B, the results of the spark ignition model represent experimental data with good accuracy. For OP B, a further investigation is needed.

To quantify the agreement between experimental data and simulation results in the main chamber, a combustion evaluation based on the mass fraction burnt (MFB) is achieved. For this purpose, three parameters are computed, namely the ignition delay (0% - 5% MFB), the center of combustion (50% MFB) and the combustion duration (5% - 90% MFB) in the main chamber. Table 3 compares the experimental and simulation results obtained for these parameters.

It can be observed that the increase of λ_{CC} increases the ignition delay. The simulated values for this parameter show a deviation of 1.2°CA with the experiments. The centre of combustion is also correctly reproduced by the simulations, with a deviation lower than 1.4°CA. Furthemore, as a mixture leaning induces a decrease of laminar flame speed, the combustion duration increases. This trend is sucessfully reproduced by the simulations. The accuracy of the simulations for this parameter is of 2.4°CA. These results meet the fundamental requirements for the modelling of this combustion process.

Table 3: Comparison of simulated and measured combustion parameters in the main chamber for the operating points OP A, OP B and OP C

OP		Ignition Delay [°CA]	Centre of Combustion [°CA aTDC]	Duration [°CA]
OP A	Exp	8.7	8.0	22.2
	Sim	8.5	8.1	24.6
OP B	Exp	9.7	8.0	27.5
	Sim	10.4	9.0	29.4
OP C	Exp	10.1	8.0	30.3
	Sim	11.3	9.4	31.6

4.3.2 Variation in engine speed

The operating points C and D represent an engine speed variation at an engine load of 100 Nm and a λ_{CC} of 2.0. This variation is used to study the impact of the turbulence in the vicinity of the spark plug on the results of the spark ignition model.

Before discussing the latters, the conditions at spark ignition timing for both operating points are considered. Fig. 6 shows the distribution of fuel mass fraction, turbulent kinetic energy (TKE), velocity at central plane and velocity field at the spark plug at spark timing for OP C and OP D, respectively. The scaling for the fuel mass fraction distribution is chosen in such a way that a stoichiometric mixture is represented by the green colour.
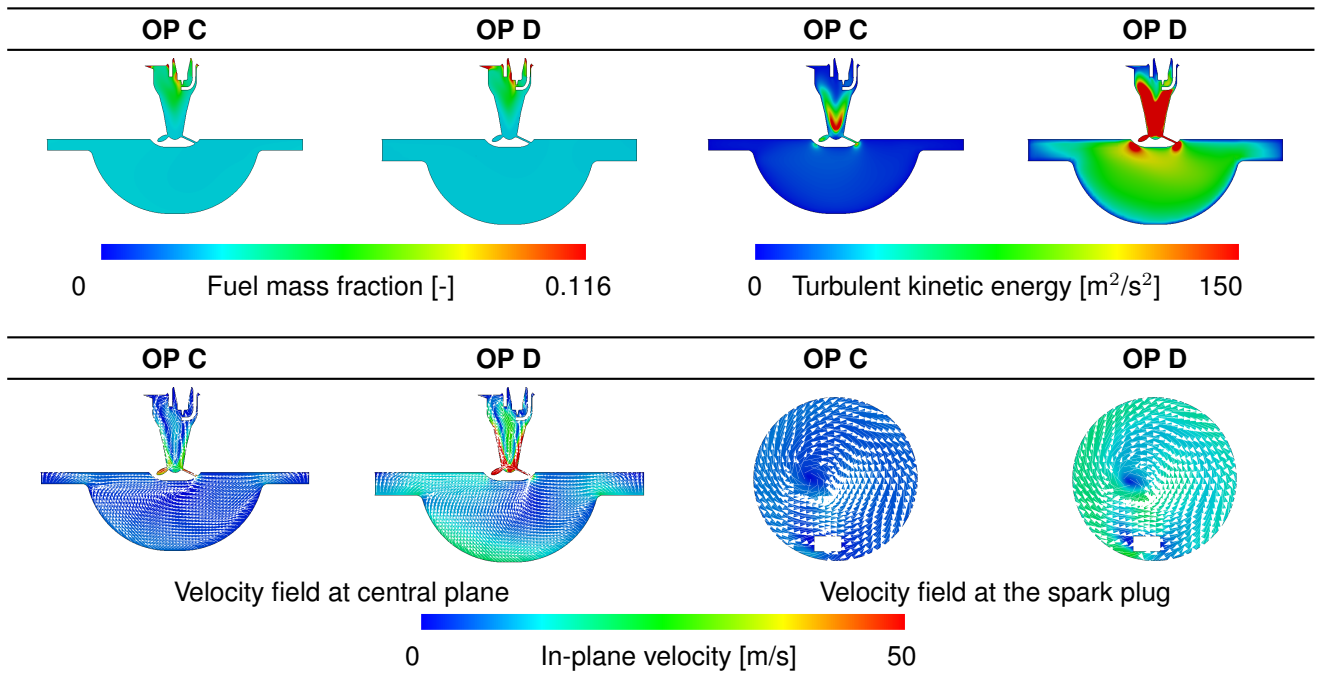
Fig. 6: Conditions at spark timing for OP C (704.5°CA Left) and OP D (695°CA Right)

Here, it is observed that for both operating points, an homogeneous mixture characterized by a λ_{CC} of 2.0 in the main chamber is retained at spark timing. The mixture in the ignition chamber is tending towards stoichiometric mixture, with some exceptional rich pockets at the top of the chamber. Around the spark plug, a stoichiometric mixture is observed. Regarding the local TKE intensity, it is observed that, with the doubling of the engine speed, the turbulence intensity in the main chamber in increased by four times. For the ignition chamber, the increase in TKE is even more intense and raises up to 6 times. A similar observation can be drawn from the comparison of the velocity field for both operating points in the two represented planes. A strong swirling motion is observed in the ignition chamber and is depicted by the velocity field at the spark plug.

Based on the previous observations, the results of the spark ignition model are analysed for both operating points. For this purpose, the computed evolution of the flame kernel radius against time after spark timing (aST) till transition into flame is shown in Fig. 7 for OP C and OP D.
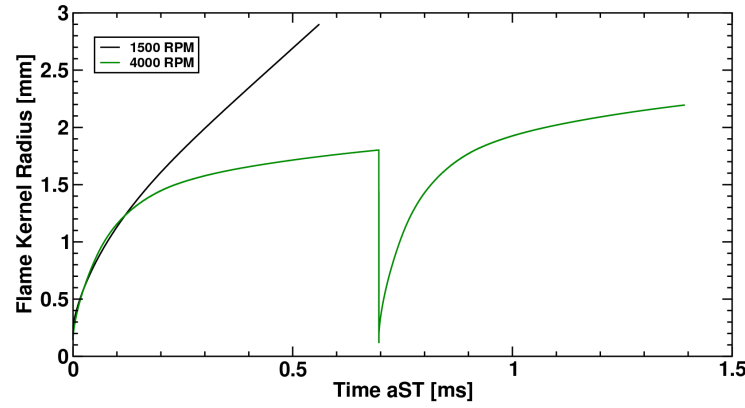
Fig. 7: Comparison of flame kernel radii for OP C (1500rpm) and OP D (4000rpm)

Here, it can be seen that, for OP C, the flame kernel has a continuous growth, while for OP D, the flame kernel initially grows, then suddenly falls down to zero, and finally again continuously grows. This particular phenomenon is called restrike, whose physical essence and modelling approach are explained in Section 3.2. Further explanations of this process can be achieved with the help of Fig. 8 and Fig. 9. The images depicted in Fig. 8 represent the spark channel elongation at spark time and 0.5ms later (0.5ms aST). The spark channel elongation is represented by means of a cluster of particles distributed along the current electrical path joining the cathode, the anode and the centre of the flame kernel, which is not represented in the images. It must be noticed that the particle size does not represent any physical property.
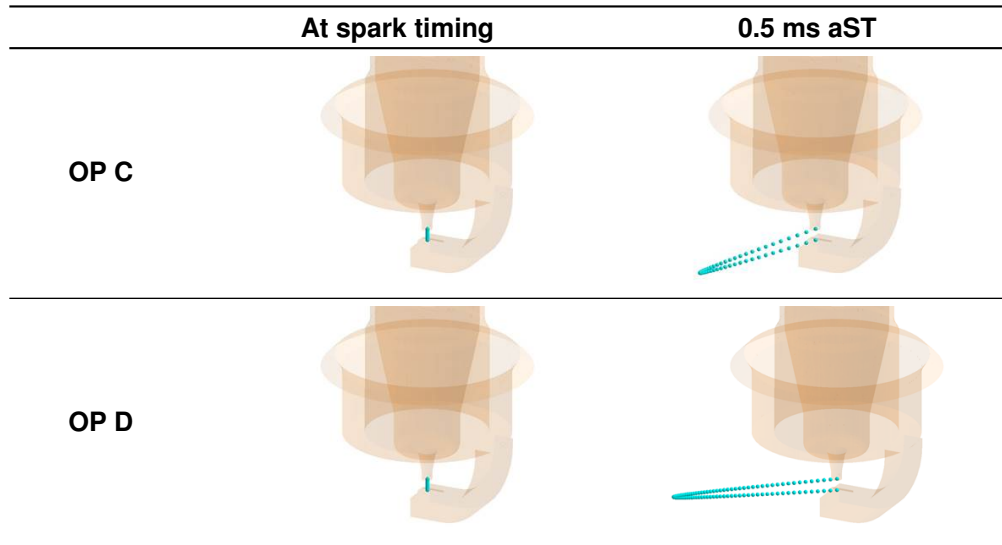
Fig. 8: Representation of the spark channel elongation for OP C (Top) and OP D (Bottom)

At spark timing, as the flame kernel is located in the centre of the electrode gap, a straight connection line is observed for both operating points. At 0.5ms aST, due to higher turbulence, a larger elongation of the spark channel is observed for OP D than for OP C. For the latter, the flame kernel growth is large enough to be transited into a flame, as shown in shown in Fig. 7. Hence the simulation with spark ignition model for this operating point is here completed.

The spark channel elongation for OP D at approximately 0.7ms aST and 1.4ms aST is illustrated in Fig. 9. These points of time correspond to the restrike and transition times, respectively. At 0.7ms aST, it is observed that, due to increased turbulence in the vicinity of the spark plug, the spark channel elongation becomes larger than the predefined value of 10 mm. Hence, restrike takes place. After this point of time, a sudden decrease in the flame kernel radius is seen, as represented in Fig. 7 for OP D. In this case, the current flame kernel is deactivated in the CFD domain, and a new one is reinitialised. At the point of transition, which is approximately of 1.4ms aST, a comparatively smaller spark channel elongation is observed than at the point of restrike, as well as a larger flame kernel growth. Under these conditions, the transition of the flame kernel into a fully propagating flame takes place. Such a flame kernel tracking can only be carried out by means of a spark ignition model.

At restrike ($\sim$ 0.7 ms aST)   **At transition ($\sim$ 1.4 ms aST)**
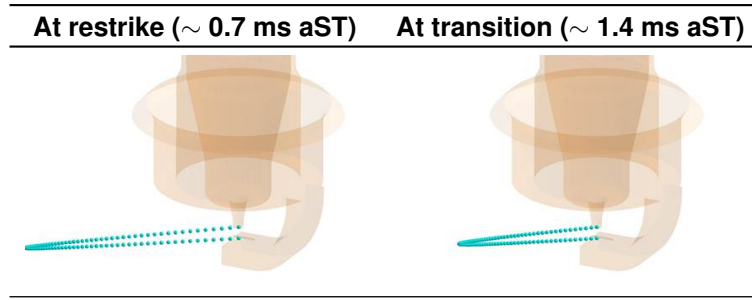

Fig. 9: Representation of the spark channel elongation for OP D at the restrike and transition times

The two sets of results conclude the model validation. The simulation setup is therefore utilised for the variation of ignition chamber design and piston bowl shape. Details of these investigations are presented in the next section.

5. Geometry variation

The validated simulation setup developed in the previous section is used to investigate the influence of the ignition chamber geometry and the piston bowl shapes, as well as their interactions, on the combustion process. For this purpose, the following iterative procedure is applied:

1. Variation of the ignition chamber design for the reference piston bowl

2. Variation of the piston bowl design for the reference ignition chamber

3. Variation of both ignition chamber and piston bowl designs

The engine operating point OP B (1500rpm, 100Nm, λ_{CC} 1.7) is simulated, which has experimentally shown the highest engine efficiency of 43% for this relative air-fuel ratio.
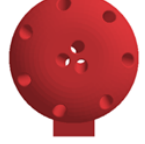
5.1. Variation of the ignition chamber design for the reference piston bowl

The design of the ignition chamber is assumed to strongly influence both ignition and combustion processes, which in the end impact the engine performance. However, the investigation of the influence of the ignition chamber design is complicated by the large number of design parameters outlined in Section 2. In order to limit the parameter space, the present analysis focuses on the number of nozzles as well as their spatial arrangement. The nozzle diameter is in all cases constant, with a value of 1.5mm.

Table 4 illustrates the investigated pre-chamber designs. As mentioned in Section 2, the reference configuration is constituted of seven regularly-spaced tilted nozzles which form a crown. The ignition chamber IC-2 differs from the reference in the orientation of the nozzles, which is only radial. The design IC-3 contains three additional nozzles oriented towards the piston, in order to better capture the bottom region of the combustion chamber. The angle between the axis of the three vertical nozzles and the chamber axis is 25°, generating thereby a dense distribution of the flame jets in this region. The latter angle is increased to 35° in the design IC-4, which therefore shows a more regular distribution of the flame jets across the combustion chamber.

Fig. 10 depicts the in-cylinder pressure and heat release rates computed for these four designs. The same simulation setup is applied for all cases. The ignition occurs at 11.5°CA bTDC. Compared to the reference ignition chamber IC-1, the radial orientation of the nozzles in the design IC-2 has a minor impact on the combustion. The peak value of the heat release rate is in this case slightly increased, but this has a very low influence on the in-cylinder pressure. The use of three additional nozzles in the designs IC-3 and IC-4 has a more significant effect on the combustion process. The simulations show a stronger pressure increase, which leads to a larger and earlier peak pressure than for the reference design. The corresponding heat release rate reveals a faster fuel conversion in the very early combustion phase, during which the flame front propagates in the ignition chamber. This rapid heat release results in an earlier flame jet exit from the ignition chamber, and therefore in a faster combustion of the mixture in the main combustion chamber.

Table 4: Investigated ignition chamber designs

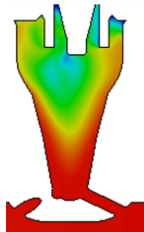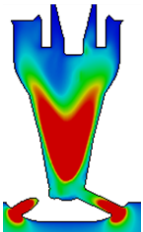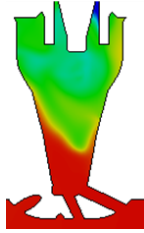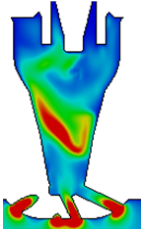| Design	Nozzles	Nozzles orientation	Side view	Bottom view
IC-1 (reference)	7	tilted		
IC-2	7	radial		
IC-3	10	tilted		
IC-4	10	tilted		
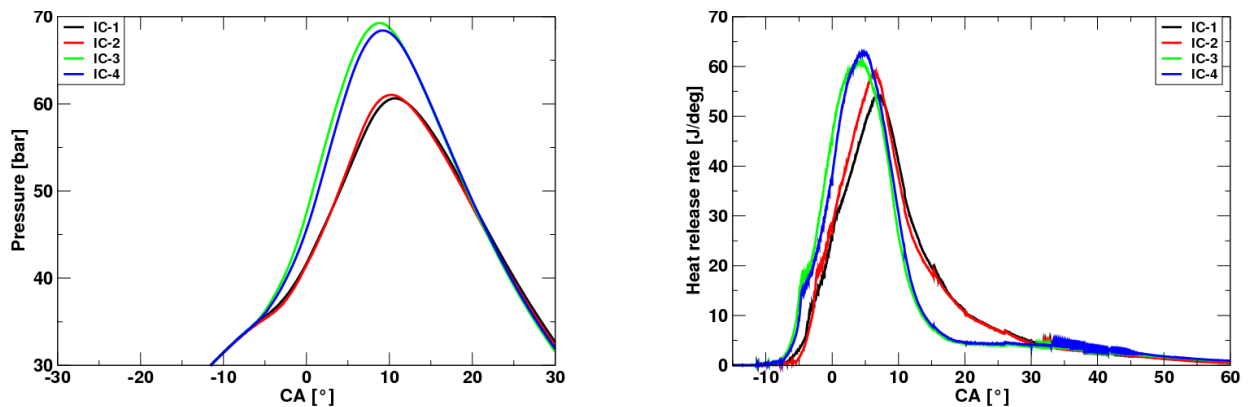
Fig. 10: Variation of ignition chamber design: in-cylinder pressure traces and heat release rates

The influence of the three additional nozzles on the combustion process within the ignition chamber is hereafter analysed. For this purpose, the fuel and TKE distributions in a middle section plot through the ignition chambers IC-1 and IC-3 at 0.5°CA before ignition are illustrated in Table 5. Both parameters are investigated as they constitute the driving forces of the flame propagation.

The geometry IC-3 shows a more homogeneous and more stochiometric mixture in the region surrounding the spark plug than in the design IC-1. On the other hand, the reference chamber IC-1 exhibits a stronger TKE level. The latter is due to the swirling flow generated within the ignition chamber by the tilted nozzles. The three additional nozzles drilled in the design IC-3 disturbs the generation of the swirling flow. This results in a lower TKE intensity within the chamber, which theoretically slows down the flame propagation. However, the flow induced by the three additional nozzles simultaneously improves the mixture formation. The more homogeneous and stroichiometric mixture explains the faster combustion progress towards the main chamber. Hence, the flame jets exit earlier from the IC-3 chamber than in the reference configuration. The mixture in the main combustion chamber is therefore ignited earlier with the IC-3 design, leading to a significant in-cylinder pressure increase. This analysis reveals that mixture formation in the ignition chamber has a more decisive influence on the combustion process than turbulence.

Table 5: Fuel distribution and turbulent kinetic energy in the ignition chambers

Design	Fuel distribution	Turbulent kinetic energy
IC-1 (reference)		
IC-3		

0.3   Lambda [-]   1.7   0   TKE [m^2/s^2]   60

Based on the previous results, it has been decided to delay the spark timing for the chamber IC-3 and IC-4 in order to obtain similar jet exit times as for the designs IC-1 and IC-2. A delay of two degrees was found to be sufficient for this purpose. This procedure ensures a good comparability of the simulation results for the analysis of the ignition chamber design on the combustion in the main chamber. The simulated in-cylinder pressures and heat release rates are illustrated in Fig. 11.
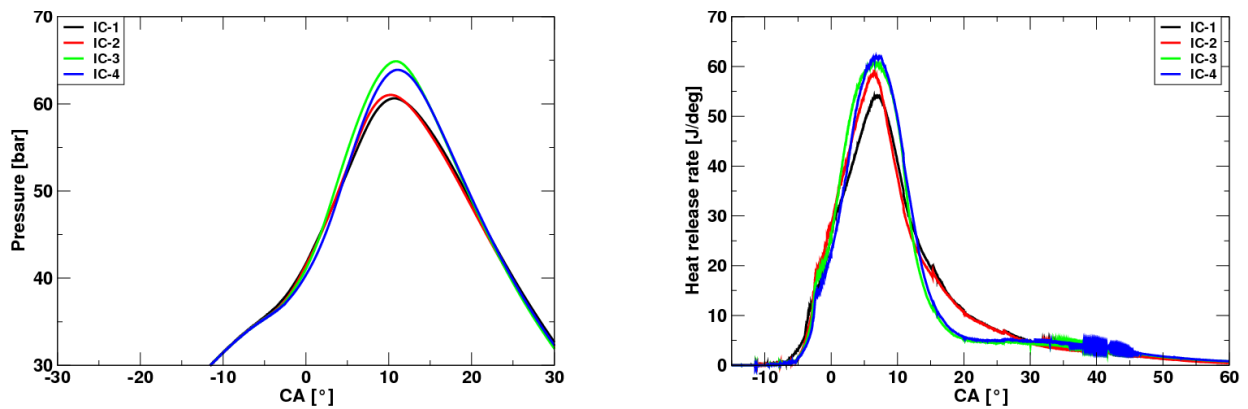
Fig. 11: Variation of ignition chamber design: in-cylinder pressure traces and heat release rates, delayed spark timing for designs IC-3 and IC-4

As expected, the four chambers present similar heat release rates and pressure increases in the short time period after spark timing. The ten-nozzle chambers then show larger pressure peaks than those constituted of seven nozzles. This effect is due to the stronger heat release until 8°CA aTDC. This increased combustion rate also explains the lower heat release observed in the late combustion phase between 13°CA aTDC and 30°CA aTDC. Regarding the ten-nozzle design, the chamber IC-3 shows a slighlty faster heat release than IC-4, which explains the earlier pressure increase.

The differences in combustion behaviour between the seven-nozzle and the ten-nozzle designs is further investigated. For this purpose, the position of the flame front at 2°CA aTDC and 10°CA aTDC for the four designs are illustrated in Fig. 12. The simulations reveal significant differences of flame front patterns between the ignition chamber designs. At 2°CA aTDC, the seven upper jets of each chamber generate a "flame crown" in the upper part of the hemispherical bowl. Each jet expands in the axial and radial directions relatively to the jet direction. The design IC-2 displays an assymetry of the jets penetration. The upper flame jets generated by the ignition chamber IC-1 and IC-2 do not reach the volume located at the bottom of the piston bowl. On the other hand, this region is already captured by the jets generated by the three vertical nozzles drilled in the ignition chambers IC-3 and IC-4. Furthermore, the dense arrangement

of the central nozzles in the design IC-3 focuses the ignition energy towards the lower part of the bowl, creating thereby a large central jet. The latter propagates rapidly towards the piston wall, and is followed by a radial expansion, which burns the volume located under the crown. The design IC-4 displays a different behaviour. The radial expansion after wall reach is not observed, due the more regular distribution of the ignition nozzles across the combustion chamber. In this case, the central jets still capture the whole volume located under the crown, but propagate axially and radially relatively to the jet direction in the same manner as the seven upper jets. These results indicate that simple variations of nozzles arrangement allows to design significantly different combustion processes. At 10°CA aTDC, it can be observed that the flame front has still not reached the volume located at the bottom of the piston bowl for the designs IC-1 and IC-2, whereas the complete piston bowl volume is burnt for the ten-nozzle designs.

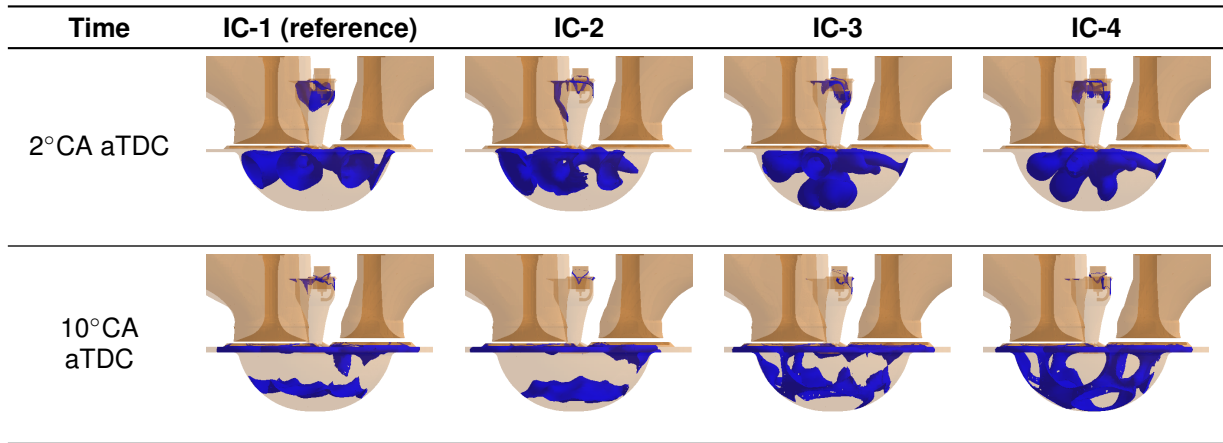| Time	IC-1 (reference)	IC-2	IC-3	IC-4
2°CA aTDC				
10°CA aTDC				

Fig. 12: Variation of ignition chamber design: flame front position, delayed spark timing for designs IC-3 and IC-4

The simulation results confirm the initially assumed strong impact of the jet nozzles number and arrangement on the combustion process. Furthermore, they demonstrate the existence of a beneficial ignition chamber design for a given piston bowl, which allows a fast heat release and an efficient late combustion phase.

5.2. Variation of the piston bowl design for the reference ignition chamber

In a similar way as in the previous section, it is assumed that the combustion process in the main chamber can be improved through modifications of the piston bowl. For this purpose, four piston shapes are investigated for a given ignition chamber, which correponds in this case to the reference design IC-1. The analysed geometries are illustrated in Table 6.

Table 6: Investigated piston bowl designs

Hemisphere (reference)	Pan
Omega	Omega-rounded
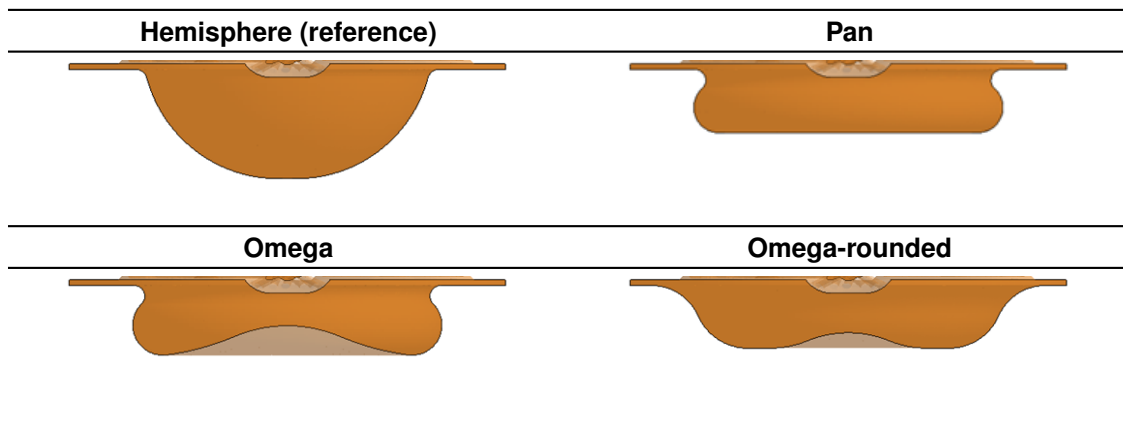
The Hemisphere, Pan and Omega designs correspond to state-of-the-art bowl shapes, which can be found in conventional diesel engines. The Omega-rounded shape has been designed to fit the flame jets pattern generated by the ignition chamber. Following this idea, the bowl volume has been concentrated away from the piston axis, while the volume under the ignition chamber has been minimized. But contrary

to the Omega design, which presents a similar feature, the Omega-rounded geometry exhibits a large rounded piston squish edge. The latter is assumed to improve the flame propagation in the liner region at the end of the combustion phase.

In order to ensure a good comparability of the results, the same computational setup and bowl volume are applied in all simulations, so that the engine compression ratio remains constant with a value of 14.5. The simulated in-cylinder pressures and heat release rates are illustrated in Fig. 13.
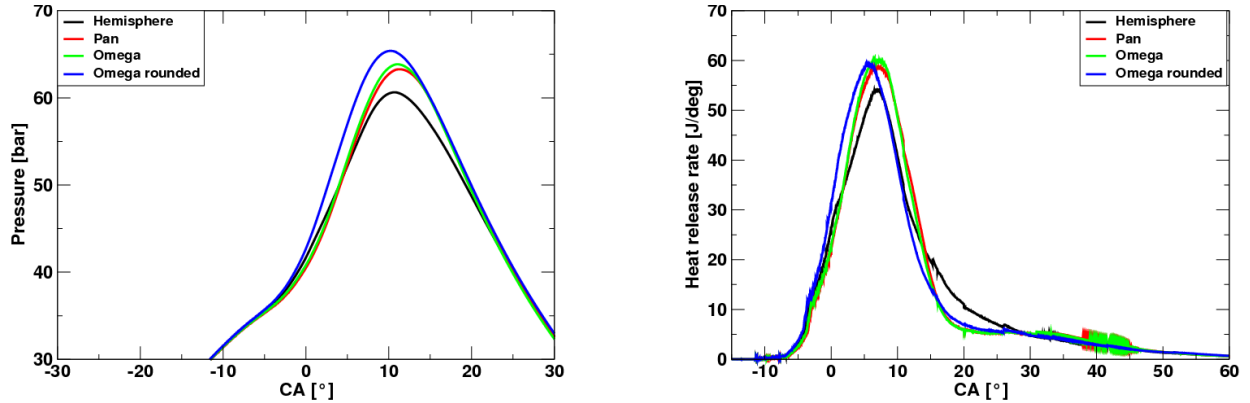

Fig. 13: Variation of piston bowl design: pressure traces and heat release rates

The Pan and Omega geometries display similar behaviours. From spark timing to 4°CA aTDC, they generate slightly smaller pressure increases than the reference hemispherical bowl. This trend is then inverted after 4°CA aTDC, where both configurations show a significantly larger pressure peak than the reference design. This increase of maximum pressure is due to a faster and stronger heat release than the reference, which also explains the lower combustion rate after 15°CA aTDC. The Omega-rounded design shows an even faster and stronger heat release than the Pan and Omega shapes, as well as a low combustion rate after 15°CA aTDC. This fast and efficient combustion generates the highest and earliest pressure peak among the four investigated designs. These simulation results confirm the hypothesis that the modification of the piston bowl geometry constitutes a significant lever to improve the combustion efficiency of pre-chamber ignited engines.

The variations of combustion efficiency between designs are hereafter analysed. For this end, the flame front progress computed for each design is illustrated in Fig. 14. As already observed in the previous section, the hemispherical bowl shows a significant unburnt volume at 2°CA aTDC in the bottom region. At the same time, the bowl volumes of the designs Pan, Omega and Omega-rounded are used in a much more efficient manner by the flame jets exiting from the ignition chamber. The dome present in the bowls Omega and Omega-rounded especially contributes to this improved volume utilisation through a lowering of the unused space. At 10°CA aTDC, the hemispherical bowl still displays a significant unburnt volume, whereas the expanding flames have reached the walls of the three other designs. The latters therefore burn a greater mixture quantitity than the reference configuration, allowing thereby a faster and stronger heat release. The Pan shape shows a small unburnt volume under the ignition chamber, which however can be considered as negligible in comparison to the one observed in the reference design. The effect of the piston squish edge rounding on the combustion is clearly visible at 80°CA aTDC. At this time, a significant flame volume can be observed in the squish region of the reference design, as well as in the Pan and Omega bowls. On the other hand, the flame front has almost vanished in the Omega-rounded design. In this case, the rounding has improved the flow close to the liner, improving thereby the combustion of the local mixture. This result confirms the assumption on the impact of piston squish edge rounding on the late combustion phase.

The improved fuel combustion in the liner region is assumed to significantly reduce Total Hydrocarbon Emissions (THC), which are considered as a critical issue in CNG engines [18]. However, the virtual analysis of this type of emissions requires a significant modelling and computational effort [19]. In order to simplify the investigations, the present paper assumes that the analysis of fresh fuel mass fraction at the end of the combustion is sufficient to qualitatively estimate the onset of THC emissions. Fig. 15 represents the temporal evolution of fresh fuel mass fraction in the end combustion phase. For the Hemisphere and Omega-rounded designs, an isosurface mapping the cells containing 100ppm of fresh fuel fraction at 80°CA aTDC is also illustrated.

The temporal evolution of fresh fuel fraction confirms the efficient fuel conversion at the end of the combustion phase in the Omega-rounded bowl. The local flow generated by the rounded piston squish edge promotes the combustion in the liner region and results in smaller unburnt fuel pockets than the reference geometry. Hence, a lower quantity of THC emissions is expected for the design Omega-rounded.
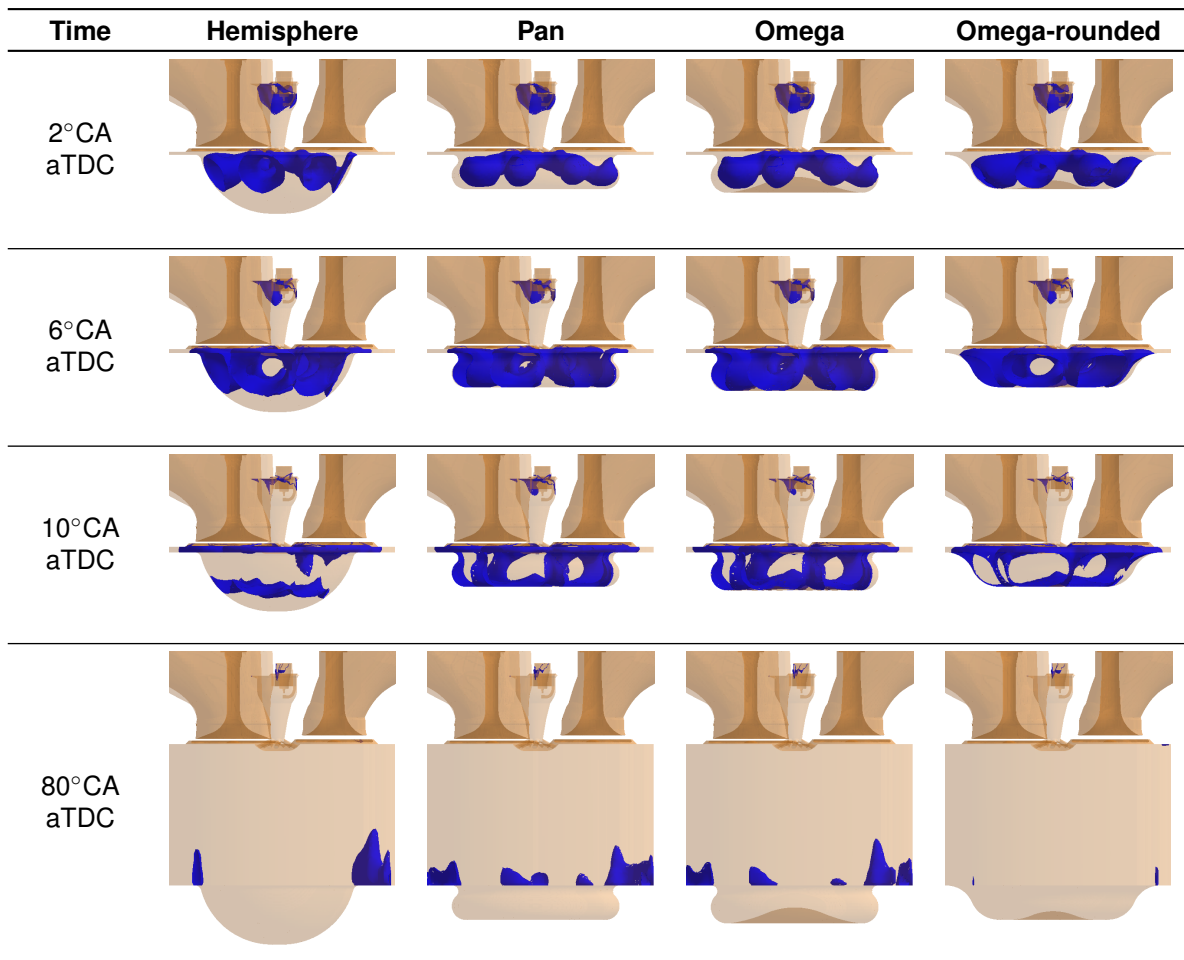
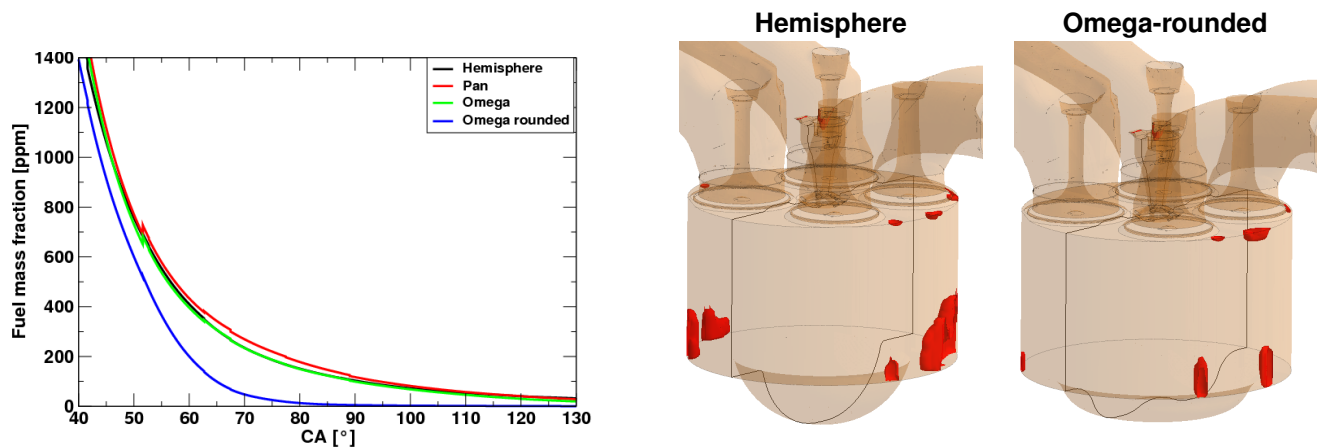Fig. 14: Variation of piston bowl design: flame front position

Fig. 15: Variation of piston bowl design: fuel mass fraction at the end of the combustion phase. Isosurface: fuel mass fraction (100ppm) at 80°CA aTDC

The CFD computations confirm the possible combustion process improvement through modifications of the piston bowl. Its shape should fit the flame jets pattern generated by the ignition chamber in order to achieve high efficiencies. A large rounded piston squish edge is also considered as beneficial for the reduction of THC emissions.

5.3. Variation of both ignition chamber and piston bowl designs

The precedent investigations have demonstrated the distinct influence of the ignition chamber and piston bowl designs on the combustion efficiency. In order to conclude the investigation, combinations of ignition

chamber and piston bowl are assessed in order to define the most advantageous ignition and combustion system. The previous variations have shown the best results for the combinations 1) ignition chamber IC-3 and reference hemispherical bowl and 2) ignition chamber IC-1 and Omega-rounded bowl. Furthermore, a rounded piston squish edge has shown promising results for the Omega-rounded bowl in terms of THC emissions. Hence, a new bowl design is introduced, which corresponds to the reference hemispherical shape with a rounded piston squish edge. The resulting matrix of ignition chambers and piston bowl combinations is given in Table 7.

Table 7: Investigated combinations of ignition chamber and piston bowl designs

			Piston bowl design	
			Hemisphere-rounded	*Omega-rounded*
Ignition chamber design	*IC-1 (reference)*		IC-1/Hemi-rounded	IC-1/Omega-rounded
	IC-3		IC-3/Hemi-rounded	IC-3/Omega-rounded

In order to ensure a good comparability of the results, the ignition is delayed by two degrees in the simulations using the ignition chamber IC-3. This ensure similar jet exit times for all ignition chambers. Fig. 16 illustrates the simulation results.
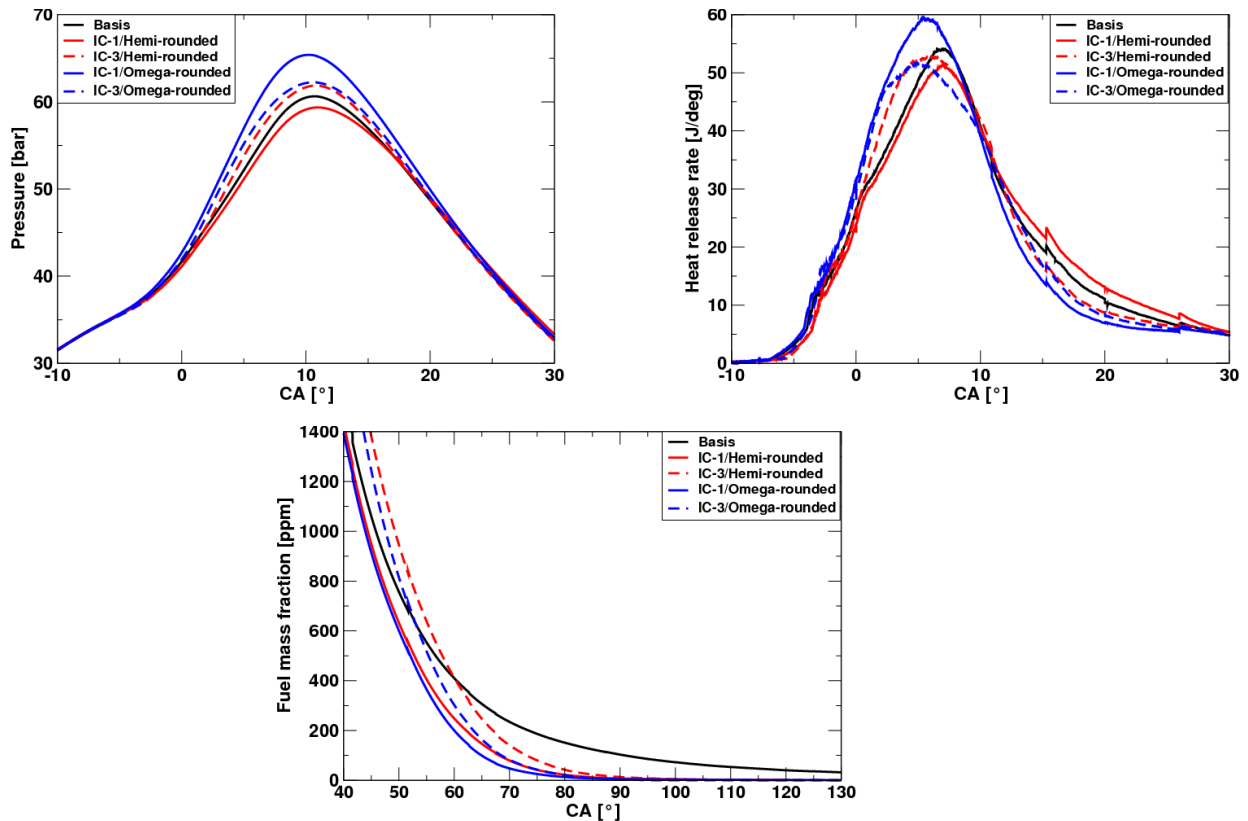
Fig. 16: Variation of piston bowl and ignition chamber designs: pressure traces and heat release rates

Until the peak at 7°CA aTDC, the IC-1/Hemi-rounded configuration shows a slightly lower heat release than the reference. Later on, the combustion rate is somewhat stronger, but the THC emissions are on the other hand clearly improved. These results therefore indicate that a largely rounded piston squish edge has a slightly negative influence on the combustion efficiency, which is compensated by a significantly positive impact on the THC emissions. The ineffectual late combustion observed in the IC-1/Hemi-rounded configuration was expected. The results presented in Section 5.1 have namely shown that combining an hemispherical bowl with the ignition chamber IC-1 is clearly not optimal. In the same manner, the better fuel combustion observed in the configuration IC-3/Hemi-rounded than in the reference design was awaited. In this case, the three additional jet flames generated by the ignition chamber IC-3 rapidly reach the bottom volume of the bowl, accelerating thereby the heat release. It is interesting to observe that the configuration IC-3/Hemi-rounded and IC-3/Omega-rounded display similar results, despite the significant heat losses engendered in the second configuration by the three central jet flames after hitting the piston dome. This negative effect on the combustion efficiency is clearly visible in the computation results obtained for the combination IC-1/Omega-rounded. After ignition, the latter design shows the fastest and strongest heat release and therefore in-cylinder pressure among all the investigated combinations, as well as the lowest combustion rate in the late phase. As this configuration also allows a significantly low level of THC emissions at the end of the combustion phase, the IC-1/Omega-rounded is considered as the the most advantageous ignition and combustion system.

6. Conclusions

The innovative monovalent CNG engine described in this paper is based on a lean combustion process. The latter uses a scavenged ignition chamber at nearly stoichiometric conditions, which delivers the required energy to ensure a stable combustion of the ultra-lean mixture. The system has been successfully integrated into the cylinder head of a VW 2.0 litre TDI® engine fuelled with an homogeneous ultra-lean mixture of air and natural gas. A preliminary CFD engine analysis based on a simple and not validated setup has resulted in a first ignition chamber design combined to a new hemispherical piston bowl geometry. This layout already delivers a break thermal efficiency of 43% on the engine test bench. In order to achieve even better performances, an effort is done to improve the CFD software VECTIS, and therefore be able to computationally improve the engine design.

For this purpose, a detailed spark ignition model considering three phases of ignition is developed. This approach is able to capture the effects of the turbulent flow field on the ignition process in the ignition chamber, and is implemented in the CFD software VECTIS. Here, with the help of lagrangian marker particles, the initial flame kernel is represented. The movement of the flame kernel due to the turbulence is then tracked. Based on the solution of the energy and mass conservation equations, the growth of the flame kernel is calculated over the spark discharge duration. Near the end of it, depending upon the size of the flame kernel and the conditions of turbulence in the proximity of the spark plug, the flame kernel is transited into a fully propagating flame.

This newly developed CFD model of ignition and combustion is validated in the target engine setup. For this purpose, a variation in the relative air-fuel ratio in the main chamber is analysed. A good qualitative and quantitative agreement is observed between the measured and simulated pressure curves in the ignition and main chambers. A variation in engine speed is then computed to further study the influence of the turbulence on the results of the spark ignition model. Here, with the increase in engine speed, an increase in the turbulence in the proximity of spark plug is observed. This leads to the event of restrike which is predicted by the advanced spark ignition model.

The validated CFD-setup is then used to analyse the influence of the ignition chamber geometry and the piston bowl shape, as well as their interactions, on the combustion process. In a first step, a variation of the ignition chamber design for the reference piston bowl is computed. The results confirm the assumed strong influence of the number of nozzles and their spatial arrangement on both ignition and combustion performance. It is observed that within the ignition chamber, mixture formation has a more decisive influence on the combustion process than turbulence. The analysis also demonstrates the existence of an advantageous ignition chamber for a given piston bowl, which allows a fast heat release and an efficient late combustion phase. The nozzles should be in this case oriented in such a way that the flame jets capture the bowl volume. In a second step, a variation of the bowl shape for the reference ignition chamber is simulated. The computations demonstrate that such modifications are able to improve the engine performance. The bowl shape should in this case match the flame jets pattern generated by the ignition chamber. The use of a large rounded piston squish edge is regarded as advantageous for the reduction of THC-emissions. A final variation of both ignition chamber and piston bowl designs is achieved in order to conclude the investigation. The simulations reveal that the combination of the reference ignition chamber and an omega bowl featuring a rounded piston squish edge corresponds to the most advantageous ignition and combustion

system among those investigated.

This promising solution has been obtained by means of a simple iterative approach. Hence, it is expected that the engine efficiency could be even further increased through an advanced optimization procedure, in which the algorithm simultaneously looks for the best design parameters for both the ignition chamber and the piston bowls.

Acknowledgements

References

[1] S. Pope. *Turbulent Flows*. Cambridge University Press, 2001.

[2] Ricardo Software. *VECTIS User Manual*. 2017.

[3] N. Peters. *Turbulent Combustion*. Cambridge University Press, 2000.

[4] B. Tao, F. Mauss, and L.M. Beck. Detailed chemistry CFD engine combustion solution with ignition progress variable library approach. *SAE Technical Paper 2009-01-1898*, 2009.

[5] R. Herweg and R. Maly. A fundamental model for flame kernel formation in s. i. engines. *SAE Technical Paper 922243*, 1992.

[6] M. Metghalchi and J.C. Keck. Burning velocities of mixtures of air with methanol, iso-octane, and indolene at high pressure and temperature. *Combustion and Flame*, 44:1081 – 1093, 1982.

[7] J. Goettgens, F. Mauss, and N. Peters. Analytic approximations of burning velocities and flame thicknesses of lean hydrogen, methane, ethylene, ethane, acetylene, and propane flames. *Symposium (International) on Combustion*, 24(1):129 – 135, 1992. Twenty-Fourth Symposium on Combustion.

[8] A. Jamrozik, W. Tutak, A. Kociszewski, and M. Sosnowski. Numerical simulation of two-stage combustion in SI engine with prechamber. *Applied Mathematical Modelling*, 37(5):2961 – 2982, 2013.

[9] S. Heyne, G. Millot, and D. Favrat. Numerical simulations of a prechamber autoignition engine operating on natural gas. *International Journal of Thermodynamics (IJoT)*, 2:43–50, 2011.

[10] R. Maly and M. Vogel. Initiation and propagation of flame fronts in lean ch4-air mixtures by the three modes of the ignition spark. *Symposium (International) on Combustion*, 17:821–831, 1979.

[11] M. Thiele, J. Warnatz, and U. Mass. 2D-simulation of ignition induced by electrical discharges. *SAE Technical Paper 1999-01-1178*, 1999.

[12] G. Tallu, L.M. Beck, M. Prouvier, A. Winkler, M. Frambourg, and E. Shapiro. 3D CFD modelling and simulation of spark ignition inclusive turbulence effects and detailed chemical kinetics. *3rd Ignition Conference, Berlin*, 2016.

[13] K. Eisazadeh-Far, H. Metghalchi, and J.C. Keck. Thermodynamic properties of ionized gases at high temperatures. *ASME Journal of Energy Resources and Technology*, 133, 2011.

[14] J. Ewald and N. Peters. Level set based flamelet model for prediction of combustion in spark ignition engines. *Interdisciplinary Aspects of Turbulence*, pages 68–76, 2005.

[15] J. Ewald and N. Peters. On unsteady premixed turbulent burning velocity prediction in internal combustion engines. *Proceedings of the Combustion Institute*, 31:3051–3058, 2007.

[16] R. Dahms. *Modeling of Combustion in Spray-Guided Spark-Ignition Engines*. Doctoral Thesis, RWTH Aachen, 2010.

[17] T. Kammermann. Internal Report : Characterisation of Ignition Process in the Ignition Cell, 2017.

[18] J.B. Heywood. *Internal Combustion Engine Fundamentals*. McGraw-Hill, 1988.

[19] T.J. Poinsot, D.C. Haworth, and G. Bruneaux. Direct simulation and modeling of flame-wall interaction for premixed turbulent combustion. *Combustion and Flame, 95:118-132*, 1993.